8th GRACM International Congress on Computational Mechanics,
Volos, 12 July - 15 July 2015

EQUILIBRIUM FLUID STRUCTURES IN PROTOTYPICAL NANOSYSTEMS

Peter Yatsyshin[1], Nikos Savva[1,2] and Serafim Kalliadasis[3]

[1]Department of Chemical Engineering
Imperial College London
London, SW7 2AZ, UK
e-mail: p.yatsyshin@imperial.ac.uk

[2]School of Mathematics
Cardiff University
Cardiff, CF24 4AG, UK

Keywords: Adsorption, Interface phase transition, Condensation, Density functional theory.

Abstract: *We present a study of liquid adsorption in narrow rectangular grooves formed by capping two parallel planar walls (a slit pore) with a third wall orthogonal to the two planar walls. By employing a fully microscopic density functional theory for classical fluids, we are able to compute the bifurcation diagrams describing the physics of wetting in narrow rectangular grooves and we demonstrate that such systems possess features common with slit pores, planar walls and wedge-shaped pores.*

1 INTRODUCTION

Investigations of fluids confined at the nanoscale are motivated by fundamental as well as applied interest. From a theoretical point of view, fluids confined in nanosystems, such as nanoscale pores, where the characteristic pore dimensions exceed the ranges of molecular interactions by only one or two orders of magnitude, are a statistical-mechanical system with a potentially rich phase behaviour, because the parameters of the fluid-substrate potential and of the pore geometry can act as thermodynamic degrees of freedom akin to temperature and pressure. In applications, enhancing our understanding of adsorption in nanoscale pores of various shapes is essential in new and rapidly developing branches of engineering and science, such as micro- and nanofluidics, biomimetics, colloidal science, design of surfaces with tuneable wetting properties and lab-on-a-chip devices [1, 2].

A satisfactory theoretical description of nanoconfined fluids has to account for the inhomogeneities of the fluid structure and the non-local character of molecular interactions. Density functional theory (DFT) for classical fluids offers a statistical mechanical framework, where the free energy of the fluid is approximated as a functional of the fluid one-body number density. Minimizing the free-energy functional yields the fluid density profile, interfaces and surface tensions while analysing the free-energy surface in the space of thermodynamic variables allows us to investigate phase transitions in the fluid and predict the formation of structures like liquid drops and films [3].

Unconstrained numerical minimisation of the model free-energy functional typically poses a non-trivial mathematical problem. The governing equations are non-local and stiff, and their numerical solution relies on finding an efficient quadrature method and ways to enhance the convergence rate of a nonlinear equation solver. A robust and efficient numerical methodology based on spectral collocation and arc-length continuation, which is applicable to a wide range of integral and integral-differential equations was proposed in our study in [4] and in some sense it can be viewed as an extension of the so-called method of van der Waals loops known in classical thermodynamics. When applied to the DFT equations, the methodology allows us to perform complex parametric studies of model systems.

Here we appropriately extend our previously developed methodology to investigate liquid adsorption in an infinite rectangular groove immersed in gas under bulk saturation. Through a parametric study of the DFT equations, we compute detailed bifurcation curves, which reveal quite an interesting physics of groove wetting. In particular, we find that different liquid structures, such as drops and slabs of liquid, can be adsorbed at the groove capping wall.

Furthermore, liquid films corresponding to the prewetting transition on the groove side walls, can be nucleated at the capping wall. As a result, prewetting transition in grooves is continuous and is manifested by the unbinding interface between thin and thick films covering the groove side walls. Our parametric study also suggests the existence of a low-temperature critical boundary separating continuous and first-order phase transitions to groove condensation. By analogy with a similar phenomenon known for wetting of planar walls, we term it "capillary wetting temperature".

2 PHYSICAL MODEL

Consider an atomic fluid in the presence of a solid substrate. The fluid–fluid and fluid–substrate molecular interactions are given by the Lennard-Jones (LJ) potential:

$$\varphi_{\varepsilon,\sigma}^{6-12}(r) = 4\varepsilon\left[-\left(\frac{\sigma}{r}\right)^{6} + \left(\frac{\sigma}{r}\right)^{12}\right], \tag{1}$$

where ε and σ control the well depth and the range of the potential, respectively. The presence of the substrate breaks the translational and rotational symmetries in the fluid. Whilst n the bulk (no substrate is present) the number density ρ of a fluid of N particles inside a volume V can be given as a scalar $\rho = N/V$, in the presence of the substrate exerting a cumulative potential $V_{\text{ext}}(\mathbf{r})$ on the fluid, the fluid density is a scalar field $\rho(\mathbf{r})$. There is a one-to-one correspondence between the fields $\rho(\mathbf{r})$ and $V(\mathbf{r})$ [5], which makes it sensible to approximate the bulk thermodynamic functions of ρ (such as, e.g., the grand potential $\Omega = -PV$, where P is the pressure) as functionals of $\rho(\mathbf{r})$ when a substrate is present. Constructing efficient and reliable approximations for thermodynamic functionals of $\rho(\mathbf{r})$ forms the subject of DFT [6].

The grand free-energy functional of the fluid in the presence of the substrate is given by

$$\Omega[\rho(\mathbf{r})] = F_{\text{in}}[\rho(\mathbf{r})] + \int \mathrm{d}\mathbf{r}\rho(\mathbf{r})\left(V_{\text{ext}}(\mathbf{r}) - \mu\right), \tag{2}$$

where integration is carried out over the domain occupied by the fluid, $F_{\text{in}}[\rho]$ is the intrinsic fluid–fluid free energy functional independent of $V_{\text{ext}}(\mathbf{r})$, and μ is the applied chemical potential, which can be viewed as a Lagrange multiplier for N [7, 8]. The equilibrium density distribution $\rho(\mathbf{r})$ minimizes $\Omega[\rho(\mathbf{r})]$, which is then equal to the grand potential Ω. The intrinsic free energy $F_{\text{in}}[\rho(\mathbf{r})]$ can be approximated by separating the fluid–fluid molecular interactions into the repulsive part acting at close range and the attractive long-range part. Considering the Lennard-Jones (LJ) molecular attractions to be added perturbatively to the purely repulsive fluid formed of hard spheres of diameter σ, one arrives at the expression [6]:

$$\begin{aligned} F_{\text{in}}[\rho(\mathbf{r})] = k_{\text{B}}T\int d\mathbf{r}\rho(\mathbf{r})\left(\ln\lambda^{3}\rho(\mathbf{r}) - 1\right) + \int d\mathbf{r}\rho(\mathbf{r})\,\psi(\rho(\mathbf{r})) \\ + \frac{1}{2}\int d\mathbf{r}\int d\mathbf{r}'\rho(\mathbf{r})\,\rho(\mathbf{r}')\,\varphi_{\text{attr}}(|\mathbf{r}-\mathbf{r}'|), \end{aligned} \tag{3}$$

where T is the fluid temperature; k_{B} and λ are the Boltzmann constant and the thermal wavelength, respectively; $\psi(\rho)$ is the configurational part of the hard sphere fluid free energy per particle [9]:

$$\psi(\rho) = k_{\text{B}}T\frac{\eta(4-3\eta)}{(1-\eta)^{2}}, \quad \eta = \pi\sigma^{3}\rho/6; \tag{4}$$

and $\varphi_{\text{attr}}(r)$ is the attractive part of the fluid–fluid moelcular potential [10]:

$$\varphi_{\text{attr}}(r) = \begin{cases} 0, & r \le \sigma \\ \varphi_{\varepsilon,\sigma}^{\text{6-12}}, & r > \sigma \end{cases}. \tag{5}$$

An expression for the cumulative substrate potential field $V_{\text{ext}}(\mathbf{r})$ completes our physical model for the fluid–substrate pair:

$$V_{\text{ext}}(\mathbf{r}) = \rho_{\text{s}}\int\limits_{v}\mathrm{d}\mathbf{r}'\varphi_{\varepsilon_{\text{s}},\sigma_{\text{s}}}^{6-12}(|\mathbf{r}-\mathbf{r}'|), \tag{6}$$

where ρ_{s} is the effective density of the substrate material, ε_{s} and σ_{s} are the parameters of the fluid–substrate LJ potential in eqn (1), and v is the volume of the LJ substrate. The formal expression in eqn (6) diverges at the

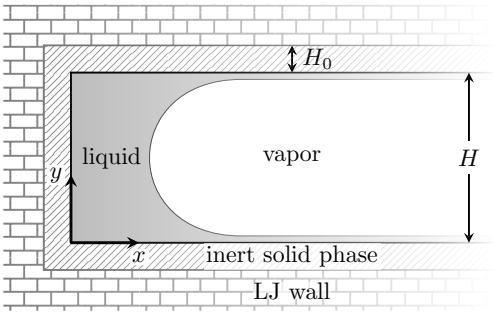

Figure 1: Groove of width H opening into a reservoir filled with gas at temperature T and chemical potential $\mu < \mu_{\text{sat}}$. The groove is transnationally invariant along the z-axis (orthogonal to the page). The LJ substrate and the inert coating of width H_0 are designated by the bricked and hatched areas, respectively. The grey-shaded area designates capillary liquid adsorbed from gas.

fluid–substrate interface, which poses numerical problems in obtaining $\rho(\mathbf{r})$. For this reason, we consider the LJ substrate to be coated with a thin layer of an inert foreign material of width H_0, which does not exert any long-ranged forces on the fluid and serves to remove the singularity of $V_{\text{ext}}(\mathbf{r})$ at the fluid–substrate contact. Thus, the integration volume v in eqn (6) excludes such coating. The coating of the substrate is not important for the physics of wetting by liquid, which is controlled by the tails of the long-ranged potentials [11]. The pore we consider in the present work is sketched in fig 1. The fluid occupies the domain $[0,\infty]\times[0,H]\times[-\infty,\infty]$ along x-, y- and z-axes, respectively, so eqn (6) takes the form:

$$V_{\text{ext}}(x,y) = \rho_{\text{s}}\int_{-\infty}^{\infty} z' \times \left(\int_{-\infty}^{\infty} x' \times \left(\int_{-\infty}^{-H_0} y' + \int_{H+H_0}^{+\infty} y'\right) + \int_{-\infty}^{-H_0} x' \int_{-H_0}^{H+H_0} y'\right) \times \varphi^{\text{6-12}}_{\varepsilon_{\text{s}},\sigma_{\text{s}}}\left(\sqrt{(x-x')^2+(y-y')^2+z'^2}\right). \tag{7}$$

For $x \to \infty$, the effect of the capping wall situated at $x = 0$ tends to be negligible, and the potential in eqn (7) reduces to the external potential of two planar walls (half-spaces filled with substrate) separated by the distance H (the so-called slit pore), i.e. $V_{\text{ext}}(x,y) \to V^{\infty}_{\text{ext}}(y)$, as $x \to \infty$, where

$$V^{\infty}_{\text{ext}}(y) = V^{(0)}_{\text{ext}}(y) + V^{(0)}_{\text{wall}}(H-y), \tag{8}$$

with the planar wall potential given by

$$V^{(0)}_{\text{ext}}(y) = 4\pi\rho_{\text{s}}\varepsilon_{\text{s}}\sigma_{\text{s}}^3\left(-\frac{1}{6}\left(\frac{\sigma_{\text{s}}}{H_0+y}\right)^3 + \frac{1}{45}\left(\frac{\sigma_{\text{s}}}{H_0+y}\right)^9\right). \tag{9}$$

2.1 GOVERNING EQUATIONS

The extremum condition, $\delta\Omega[\rho]/\delta\rho = 0$, is expressed by the following Euler-Lagrange equation for $\rho(\mathbf{r})$:

$$k_{\text{B}}T\ln\rho(\mathbf{r}) + \psi(\rho(\mathbf{r})) + \rho(\mathbf{r})\,\psi'_{\rho}(\rho(\mathbf{r})) + \int \mathrm{d}\mathbf{r}'\rho(\mathbf{r}')\,\varphi_{\text{attr}}(|\mathbf{r}-\mathbf{r}'|) + V_{\text{ext}}(\mathbf{r}) - \mu = 0, \tag{10}$$

where $\psi'(\rho)$ denotes the derivative of $\psi(\rho)$ with respect to ρ. For fixed T we can obtain a set of solutions, $\{\rho(\mathbf{r})\}_{\mu}$, to the above equation parametrized by μ. This allows us to apply the apparatus of classical thermodynamics, namely, the method of van der Waals loops [7], to analyse the stability of different fluid configurations obtained numerically from eqn (10). In equilibrium, the grand potential $\Omega(\mu)$ is a concave function of μ, so the density profiles which satisfy eqn (10) and correspond to stable (and metastable) fluid configurations, also correspond to concave branches of $\Omega[\{\rho(\mathbf{r})\}_{\mu}]$ as a function of μ. The stable configurations (but not the metastable ones) also form the lower envelope of $\Omega[\{\rho(\mathbf{r})\}_{\mu}]$ as a function of μ. Thus, there are good physical reasons to consider bifurcation curves of eqn (10) for various fixed values of T in terms of the so-called isotherms of the grand potential $\Omega(\mu) = \Omega[\{\rho(\mathbf{r})\}_{\mu}]$.

The main strength of the method of van der Waals loops is that it can be used to identify phase transitions, i.e. co-occurrence of two (or more) topologically different fluid configurations, $\rho_1(\mathbf{r})$ and $\rho_2(\mathbf{r})$, at the same values of

T and μ. For fixed T such coexisting fluid configurations belong to the set $\{\rho(\mathbf{r})\}_\mu$ and correspond to μ, such that $\Omega(\mu)$ is non-analytic. A first-order and a continuous phase transition are characterized by a jump discontinuity and a singularity of the derivative of $\Omega(\mu)$ with respect to μ, respectively. During a first-order transition, $\rho_1(\mathbf{r})$ and $\rho_2(\mathbf{r})$ satisfy the following system of equations

$$\begin{gathered}\left.\frac{\delta\Omega[\rho_1(\mathbf{r})]}{\delta\rho}\right|_{\rho_1(\mathbf{r})} = \left.\frac{\delta\Omega[\rho_1(\mathbf{r})]}{\delta\rho}\right|_{\rho_2(\mathbf{r})} = 0 \\ \Omega[\rho_1(\mathbf{r})] - \Omega[\rho_2(\mathbf{r})] = 0,\end{gathered} \tag{11}$$

which expresses the geometrical condition of self-intersection of two branches of $\Omega(\mu)$. For example, in the bulk, eqs (11) provide the condition of saturation, i.e. coexistence of the vapour and liquid. Setting $V_{\text{ext}} \equiv 0$ in eqs (11), we get

$$\begin{gathered}\mu = k_{\text{B}}T\ln\rho + \psi(\rho) + \rho\psi'_\rho(\rho) - \tfrac{32\pi}{9}\rho\sigma^3\varepsilon, \\ P = \rho k_{\text{B}}T\tfrac{1+\eta+\eta^2-\eta^3}{(1-\eta)^3} - \tfrac{16\pi}{9}\rho^2\sigma^3\varepsilon.\end{gathered} \tag{12}$$

The saturation densities of vapour, ρ_{vap}, and liquid, ρ_{liq}, at T and $\mu_{\text{sat}}(T)$ can then be found from the balance $\mu(\rho_{\text{liq}}) = \mu(\rho_{\text{vap}}) = \mu_{\text{sat}}$ and $P(\rho_{\text{liq}}) = P(\rho_{\text{vap}}) = P_{\text{sat}}$, where P_{sat} is the pressure at saturation.

When the substrate is present, it is often convenient to split the grand potential into the bulk and excess contributions, so that for different fluid phases of interest (e.g., drops in the corners of the groove capping wall, liquid slabs adsorbed on the capping wall, etc) the bulk parts of Ω are equal, but the excess parts are different, unless a phase transition is taking place [12]. The obvious choice is to relate the excess grand potential to that of a slit pore of the same width:

$$\Omega^{\text{ex}} = \Omega[\rho(x,y)] - \Omega[\rho^\infty(y)], \tag{13}$$

where $\Omega[\rho(x,y)]$ and $\Omega[\rho^\infty(y)]$ are computed using eqn (2) from the fluid density distributions $\rho(x,y)$ and $\rho^\infty(y)$ inside the groove and inside the slit pore, respectively. Since $\rho(x,y) \to \rho^\infty(y)$, as $x \to \infty$, the expression in eqn (13) is finite.

3 NUMERICAL APPROACH

Let us discuss the numerical challenges associated with solving eqs (10) and (11) in two dimensions. Over the years, a number of numerical approaches have been proposed for the non-local integral equations of DFT [13–17]. The crucial step is to accurately and efficiently compute the integral terms, such as those corresponding to fluid–fluid interactions [see, e.g., the fourth term in eqn (10)]. Our recent studies of local/differential equations [18, 19] and non-local/integral equations [3, 4, 20] highlight the advantages of employing pseudospectral collocation methods [21, 22]. In integral equations we use the Clenshaw–Curtis quadrature to evaluate the non-local terms [4, 23]. It is noteworthy that a properly implemented spectral method has an exponential convergence rate with the size of the computational mesh. At the same time, other commonly used approaches, such as those based on the Simpson rule or the fast Fourier transform only have algebraic convergence [14, 24]. The faster convergence rate of the spectral method allows us to use significantly fewer mesh points when discretising the computational domain, while retaining high accuracy of the computations. This is especially important for solving two-dimensional (2D) problems.

In order to solve eqs (10) and (11) pseudospectrally, the unknown density $\rho(\mathbf{r}) \equiv \rho(x,y)$ is discretized on a non-uniform mesh of collocation points, where a global interpolating function is constructed. The pseudospectral method developed for integral-differential equations in reference [4] was extended for the purposes of the present study to 2D problems by constructing the global interpolant on a tensor product mesh of Chebyshev collocation points [22], which are mapped conformally onto the physical domain of interest. Mathematical operations performed on the global interpolant have exponential accuracy. The benefit of using conformal maps is that we can position the collocation points densely near the substrate walls, where $\rho(x,y)$ is expected to vary steeply, while far from the walls we can use a coarser mesh. In practice, when discretizing the domain inside the groove in fig 1, we positioned the last point at a distance of about $10^3\sigma$ from the capping wall and used mesh sizes of 130 and up to 60 points along the x- and y-directions, respectively. Discretizing eqs (10) and (11) leads to systems of non-linear algebraic equations, which are solved using Newton's algorithm. A tolerance of 10^{-7} typically requires around 2 or 3 iterations. The calculation time is significantly reduced by evaluating the non-local integral term as a matrix-vector product, where the matrix is computed outside the Newton loop.

Fig 2 shows the results of a convergence test for the numerical solver of eqn (10) for a groove with $H = 30$ and two different sets of fluid–substrate parameters: $\varepsilon_{\text{s}} = 0.6\varepsilon$, $\sigma_{\text{s}} = 1.7\sigma$, $H_0 = 3.5\sigma$ (black) and $\varepsilon_{\text{s}} = 0.7\varepsilon$,

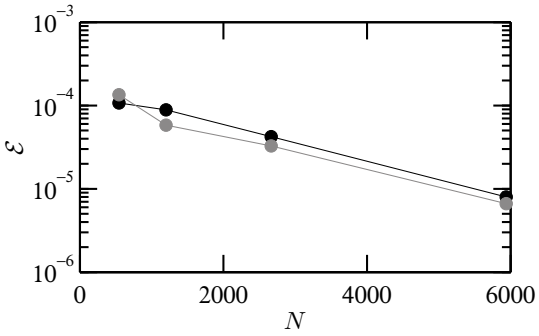

Figure 2: Convergence of the numerical scheme [see eqn (14)] with the number N of mesh points.

$\sigma_s = 2\sigma$, $H_0 = 5\sigma$ (grey). A density profile $\rho_0(x, y)$ of a fluid configuration similar to the one shown in fig 3(c), with the center of the meniscus along the x-axis located at approximately 10σ from the capping wall, was obtained on the reference grid with 162×80 points along the x- and y-axes, respectively. The same calculation was repeated on coarser meshes of size 32×16, 48×24, 72×36 and 108×54 obtaining $\rho_N(x, y)$, where N is the total number of mesh points. To compare $\rho_N(x, y)$ with $\rho_0(x, y)$, we interpolated both solutions on a truncated domain $[0, 20] \times [0, 30]$, which was discretized uniformly with $K = 2400$ points, using 2 points per σ along each dimension. The estimate of the average error is given as the mean of the Euclidean norm of the difference of the interpolated data, namely

$$\mathcal{E} = \frac{1}{K}\sqrt{\sum_{i=0}^{K}[\rho_N^{(i)} - \rho_0^{(i)}]^2}, \tag{14}$$

where the superscript (i) is a label for points on the uniform grid.

Apart from the discretisation issues, there is a considerable challenge in selecting an initial guess for the Newton algorithm (or any other iterative scheme, e.g., Picard) to converge. We overcome it by employing a pseudo arc-length continuation technique [4, 25], which allows us to treat any parameter in the non-linear system of equations as an unknown, and serves to optimize the selection of the initial guess. In eqn (10) we choose μ as the continuation parameter and start our calculations at a rather low value of μ, where the fluid is a dilute gas, so a simple initial guess suffices to obtain the unique numerical solution. The continuation algorithm then proceeds to automatically vary the values of μ and provide an optimal initial guess for the Newton method to converge for every successive value of μ. This allows us to obtain the grand potential isotherms in a systematic and efficient fashion. By applying the same method to eqs (11), we can trace the transitions with T as the continuation parameter, and construct the phase diagrams of various transitions. All computations presented in the following section were done on a standard desktop computer. In practice, the calculation of a single density profile $\rho(x, y)$ from eqn (10) takes about a minute, and the calculation of a phase diagram from eqs (11), with T treated as a parameter, takes about two hours.

4 RESULTS AND DISCUSSION

In what follows, we set the parameters ε and σ in eqn (5) as units of length and energy. Computing the bulk saturation curve using eqs (12), we find the critical temperature of liquid–vapour coexistence at $T_c = 1.006\varepsilon/k_B$ [4]. Since we study systems under saturation, i.e. such that at any given T in eqn (10), $\mu < \mu_{sat}(T)$, it is convenient to define the disjoining chemical potential $\Delta\mu = \mu - \mu_{sat} < 0$, which we will use for plotting the bifurcation diagrams. In eqn (6) we set $\rho_s = 1$ and choose the parameters $\varepsilon_s = 0.7$, $\sigma_s = 2$ and $H_0 = 5$, so that planar wetting is first-order (see, e.g., [4,26]), with a relatively high value of planar wetting temperature $T_w = 0.755$ (T_w provides the lower limit of temperatures at which the contact angle of a macroscopic sessile drop sitting on a planar wall surface is zero [4, 26]). We prefer T_w to be high, so that liquid–gas interfaces are not very steep, for numerical convenience. In this section we consider in detail a particular case of the groove of width $H = 40$, because it exhibits rather interesting picture of fluid phase behavior. A comment on what should be expected at smaller and higher values of H is provided at the end of the present section.

Setting $T = 0.87$ (a more or less randomly chosen value just below T_w), we apply arc-length continuation in μ to equation (10), and compute a set of density profiles $\{\rho(x, y)\}_\mu$, together with the corresponding bifurcation curve expressed in terms of the grand potential isotherm $\Omega^{ex}(\mu) = \Omega^{ex}[\{\rho(x, y)\}]$, see eqn (13). The thermodynamic

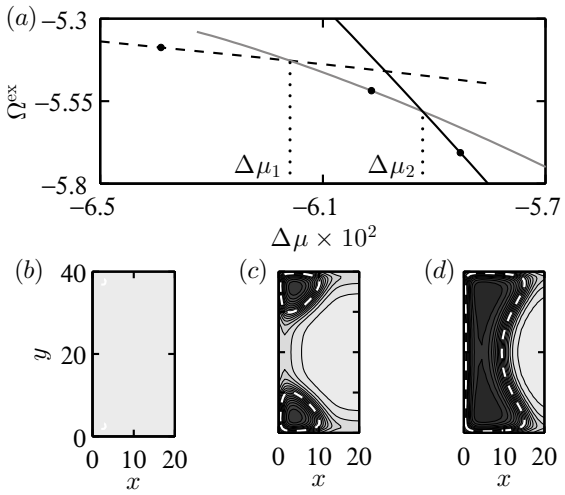

Figure 3: Stable phases in a groove of width $H = 40$ at $T = 0.87$, and with the fluid–substrate potential parameters $\varepsilon_s = 0.7$, $\sigma_s = 2$, $H_0 = 5$. (a) Concave branches of $\Omega^{ex}(\mu)$ corresponding to gas (dashed), drops (solid grey) and liquid slab (solid black). The Gas–drop and drop–slab transitions take place at $\Delta\mu_1 = -6.15 \times 10^{-2}$ and $\Delta\mu_2 = -5.92 \times 10^{-2}$, respectively. Condensation is at $\Delta\mu_c = -3.89 \times 10^{-2}$. Circles designate representative density profiles inside each phase, which are plotted in (b)–(e). The data is scaled between $\rho_{vap} = 0.06$ (light grey) and $\rho_{liq} = 0.06$ (dark grey), with a sharp interface (dashed white curve) along the contour of $(\rho_{vap} + \rho_{liq})/2$.

stability requirement, expressed by the concavity of the different branches of $\Omega^{ex}(\mu)$, allows us to discard the solutions of eqn (10), which do not minimize the grand-free energy, and we are left with a manifold of stable (and metastable) fluid configurations. The calculation is summarized in fig 3, and allows us to identify for the chosen T three distinct fluid phases, which correspond to the concave branches of $\Omega^{ex}(\mu)$ [see fig 3(a)]: gas (dashed), liquid drops in the groove corners (solid grey) and liquid slab at the groove capping wall (solid black). The representative fluid density profiles inside each phase are shown in figs 3 (b)–(d) on a grey scale, where light and dark grey correspond to $\rho_{vap} = 0.06$ and $\rho_{liq} = 0.5$, respectively, and the sharp liquid–gas interface is defined along the contour of $(\rho_{vap} + \rho_{liq})/2$.

The computed bifurcation curve $\Omega^{ex}(\mu)$ reveals the physics of fluid behavior inside the groove, as μ is increased from a large negative value corresponding to bulk gas in the direction of bulk liquid–vapour coexistence. At low negative $\Delta\mu$, the fluid inside the groove is in the gas phase. When $\Delta\mu$ is increased, the gas becomes denser, and a first-order transition from gas to two drops in the corners can take place as result of a thermal fluctuation anywhere in the region where the dashed and solid grey phase-branches overlap. The most likely transition point is at the intersection of the phase-branches, at $\Delta\mu_1 = -6.15 \times 10^{-2}$. The same can be said about the transition of the drop phase to the liquid slab phase, which is most likely to take place at $\Delta\mu_2 = -5.92 \times 10^{-2}$. Above $\Delta\mu_2$, increasing $\Delta\mu$ results in the growth of the adsorbed liquid slab, which then fills the groove continuously. There is an upper limit at $\Delta\mu_c = -3.89 \times 10^{-2}$, where the groove is entirely filled by liquid. The derivative of $\Omega^{ex}(\mu)$ with respect to μ has a singularity at μ_c, which thus corresponds to the continuous phase transition.

The value of $\Delta\mu_c$ can be found independently, by considering phase transitions in the fluid inside a slit pore of the same width. This is not surprising, since according to eqs (7) and (8), the slit pore provides a topological limit for the groove. It is well known that gas and liquid inside a slit pore can transform during the condensation transition at μ_c [12, 26, 27]. Noteworthy is that, just like saturation in the bulk, condensation in slit pores is always a first-order transition. From that point of view it is quite interesting to find that capping a slit pore to form a groove can change the order of condensation to continuous as manifested by the liquid slab continuously filling the groove in the limit $\mu \to \mu_c$ [3, 12].

Intersections of branches of $\Omega^{ex}(\mu)$ are described by eqs (11). Applying continuation in T to eqs (11), we can trace the phase transitions with temperature and construct the so-called thermodynamic phase diagram of different fluid phases inside the groove. Fig 4 summarises a complex parametric study of various phase transitions possible in our groove. Two first-order transitions described above and summarised by fig 3 correspond to crossing curves 5 and 6 in fig 4 vertically at $T = 0.87$. Yo make sense of the complex physical picture provided by the calculation, we must make the connection with the wetting phenomenology of the topologically limiting systems of the groove. As we have seen, in the limit $x \to \infty$ the groove becomes equivalent to the slit pore. The limit $y \to \infty$ with the

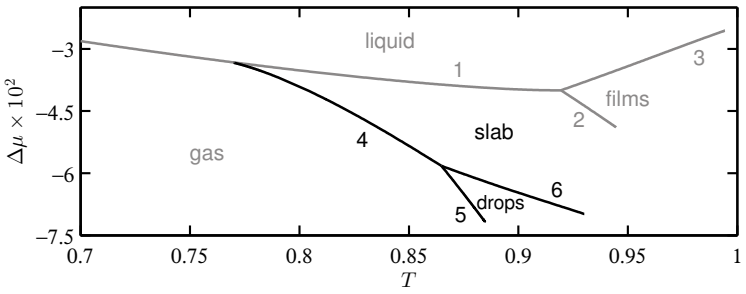

Figure 4: Phase diagram of transitions in the groove from fig 3. Black and grey colors correspond to transitions occurring near the groove capping wall and those occurring in the groove volume, respectively. The latter also occur in the slit pore of the same width. 1 and 3: condensation curve $\mu_{\rm c}(T)$; 2: remnant prewetting on the side walls; 4 and 6: capillary prewetting $\mu_{\rm cpw}(T)$, which joins condensation tangentially at $T_{\rm cw} = 0.770$; 5: remnant corner prefilling.

origin fixed reduces the groove to a right-angled corner or wedge. Finally, in the double limit $x \to \infty$ and $y \to \infty$ the groove is reduced to a single planar wall. As we will see, the most important analogy is that with a slit pore. For this reason, the different transition curves and labels marking the regions of phase stability in figure 4 are coloured black for the transitions associated with the groove capping wall, and grey for the transitions that also occur in a slit pore of the same width (like condensation discussed above).

Let us first discuss briefly the fluid phase transitions taking place in a slit pore. As we will see below, these transitions are continuous in the groove. Curves 1 and 3 form the condensation curve $\mu_{\rm c}(T)$ discussed above, where inside the pore gas transforms into liquid during a first-order transition. Curve 2 corresponds to an additional transition, which occurs here due to the particularly large value of H. In sufficiently wide slit pores, the side walls of the pore can adsorb liquid films below condensation [27]. Film adsorption is typical of isolated planar substrates [such as the one described by the potential $V_{\rm ext}^{(0)}$ in eqn (9)], where it can give rise to the first-order prewetting transition manifested by a jump in the thickness of the adsorbed film at some $\mu_{\rm pw}$ [26]. The prewetting transition curve of a single planar wall, $\mu_{\rm pw}(T)$, joins saturation tangentially at the wall wetting temperature $T_{\rm w}$, where also the thickness of the thick film, coexisting with the thin film during prewetting, is infinitely large, while the thickness of the thin coexisting film is mesoscopic [4, 12, 26]. In a slit pore, bulk saturation is pre-empted by condensation, which affects the $\mu_{\rm pw}(T)$-curve, shifting and shortening it as demonstrated in fig 4, where the transition curve 2 is the remnant of the single wall prewetting. The triple point at $T_3^\infty = 0.920$ belongs to all three curves 1–3, and is characterized by the fact that gas, films and liquid have the same energy, and are, thus, equally probable to be observed.

Capping the slit pore to form the groove gives rise to the transition curves 4-6, which repeat the pattern set by the grey curves 1-3. Note, that curve 4, along which gas coexists with the slab-phase, is tangential to condensation [12]. Moreover, along curve 4, the length of coexisting capillary liquid slab grows closer to condensation and is infinite at the common point of curves 4 and 1 [3, 12]. In this respect, curve 4 is equivalent to planar prewetting described above. Extending this analogy, we can term curves 4 and 6 "capillary prewetting", $\mu_{\rm cpw}(T)$, and the temperature at which $\mu_{\rm cpw}(T)$ tangentially approaches $\mu_{\rm c}(T)$, "capillary wetting temperature", $T_{\rm cw}$. In fact, condensation in grooves is continuous at $T > T_{\rm cw}$, and is first-order at $T < T_{\rm cw}$ [3, 12].

The appearance of drops in the corners of the groove is in fact a remnant of the corner prefilling transition, which occurs in wedge-shaped pores and is manifested by the coexistence of gas with a drop adsorbed in the wedge apex [28, 29]. In the groove we consider, the remnant corner prefilling appears as transition curve 5 demarcating the region of stability of the drop phase. The interplay of corner prefilling with capillary prewetting results in the appearance of the triple point at $T_3 = 0.865$ where gas, corner drops and a slab of finite length have equal energies.

The phase diagram of the groove in fig 4 is in fact an interesting, but a quite particular case, where the transitions specific to various topological limits of the groove are well manifested. In very narrow grooves, the capillary effects of the so-called Kelvin shift of the bulk saturation [12, 27] are quite important, and lead to the remnant corner prefilling being pre-empted by condensation, so curve 5 is not present at small H. At large H, the Kelvin shift is minimal, and as a result, the condensation curve $\Delta\mu_{\rm c}(T)$ tends to the bulk saturation line $\Delta\mu = 0$. At the same time, the corners of the groove are quite isolated, and the remnant corner prefilling curve 5 should have a common point with the saturation curve somewhere below $T_{\rm cw}$, which in this limit tends to the planar wetting

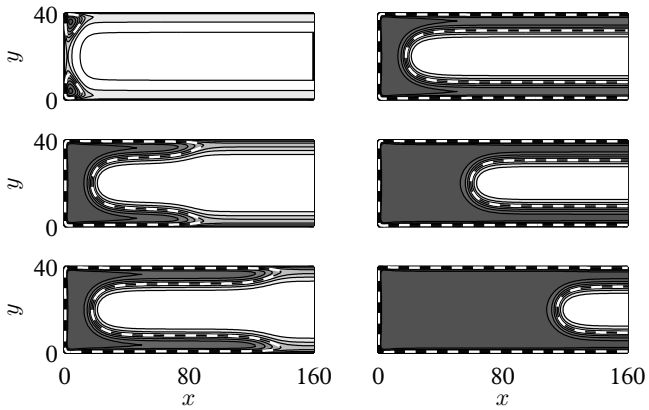

Figure 5: Fluid configurations in the groove at $T = 0.93$, during continuous prewetting at $\Delta\mu_{\rm pw} = -4.367 \times 10^{-2}$ (left column of plots) and continuous condensation $\Delta\mu_{\rm c} = -3.802 \times 10^{-2}$ (right column of plots). The values of $\Delta\mu$ corresponding to the left column (top to bottom): $(-8.282; -4.380; -4.373) \times 10^{-2}$. Same for the right column (top to bottom): $(-4.367; -3.815; -3.804) \times 10^{-2}$.

temperature $T_{\rm cw}$. So the triple point of curves 4, 5 and 6 disappears for large H. The triple point of curves 1, 2 and 3, on the other hand, remains in the limit of large widths.

Let us now illustrate the continuous transitions in the groove by computing an isotherm at $T = 0.93$, across transition curves 2 and 3 in fig 4. Representative density profiles are given in fig 5, where the left and right columns of plots correspond to $\mu < \mu_{\rm pw}$ and $\mu_{\rm pw} < \mu < \mu_{\rm c}$, respectively. The data is scaled between $\rho_{\rm vap} = 0.09$ (white) and $\rho_{\rm liq} = 0.40$ (dark grey). In the left column of plots we observe a nucleation and unbinding of prewetting films on the groove side walls as $\Delta\mu$ is increased, so that in the limit $\mu \to \mu_{\rm pw}$, the side walls are completely covered by the prewetting films. Noteworthy is that the circular-arc meniscus in the center of the groove remains pinned near the capping wall, while the prewetting film unbinds. At $\mu > \mu_{\rm pw}$, the meniscus depins and starts to unbind from the capping wall manifesting continuous condensation, which occurs in the limit $\mu \to \mu_{\rm c}$.

5 CONCLUSIONS

The behavior of fluids in nano-pores is determined by a complicated interplay between molecular fluid–fluid and fluid–substrate interactions. Unravelling the various wetting mechanisms can only be achieved through detailed computations or carefully set up experiments. In the present work we performed a detailed and systematic parametric study of the DFT model of adsorption for an illustrative case study of a 2D rectangular groove. Most of the technical complexity of the approach can be encapsulated within our previously developed numerical methodologies [4], as they provide the means to obtain the phase portrait of the system under consideration in a systematic manner. This allows us to argue in terms of the fluid structure and its phenomenology, and elucidate the connections between the physics of wetting of different systems.

It is important to emphasize that in the present work we neglected the fluctuations of the fluid density along the z-axis (see fig 1), and for that reason we also did not discuss the critical points at the high-temperature ends of various transition curves presented in fig 4. Indeed, including fluctuations requires a non-classical approach beyond DFT, and is of separate interest [8]. Other studies expanding the present investigation may include wetting of non-homogeneous grooves with corrugated or chemically decorated walls or investigation of layering transitions on the side walls, which may occur continuously, similarly to prewetting. The ramifications of multiple fluid phase equilibria for lowering the nucleation barriers and various other dynamic processes are also of interest, and may be investigated using dynamic DFT models, such as, e.g., those developed by Goddard et al. [30, 31].

Acknowledgments
This work is supported by the European Research Council through Advanced Grant No. 247031.

References

[1] Herminghaus, S., Brinkman M., and Seeman, R. (2008), "Wetting and Dewetting of Complex Surface Geometries," *Annu. Rev. Mater. Res.*, Vol. 38, p. 101.

[2] Bonn, D., Eggers, J., Indekeu, J., Meunier, J. and Rolley, E. (2009), "Wetting and Spreading," *Rev. Mod. Phys.*, Vol. 81, p. 739.

[3] Yatsyshin, P., Savva, N. and Kalliadasis, S. (2013), "Geometry-Induced Phase Transition in Fluids: Capillary Prewetting," *Phys. Rev. E*, Vol. 87, p. 020402(R).

[4] Yatsyshin, P., Savva, N. and Kalliadasis, S. (2012), "Spectral Methods for the Equations of Classical Density-Functional Theory: Relaxation Dynamics of Microscopic Films," *J. Chem. Phys.*, Vol. 136, p. 124113.

[5] Mermin., N. D. (1965), "Thermal properties of the inhomogeneous electron gas," *Phys. Rev.*, Vol. 137, p. A1441.

[6] Lutsko, J. F. (2010), *Recent Developments in Classical Density Functional Theory*, in *Adv. Chem. Phys.*, p. 1, John Wiley & Sons.

[7] Callen, H. B. (1985), *Thermodynamics and an Introduction to Thermostatistics*, John Wiley & Sons.

[8] Hansen, J. and McDonald, I. (2006), *Theory of Simple Liquids (3rd edn)*, Elsevier.

[9] Carnahan, N. F. and Starling, K. E. (1969), "Equation of State for Nonattracting Rigid Spheres," *J. Chem. Phys.*, Vol. 51, p. 635.

[10] Barker, J. A. and Henderson, D. (1967), "Perturbation Theory and Equation of State for Fluids. II. A Successful Theory of Liquids," *J. Chem. Phys.*, Vol. 47, p. 4714.

[11] Sullivan, D. E. and Telo da Gama, M. M. (1986), *Wetting Transitions and Multilayer Adsorption at Fluid Interfaces,* in Croxton, C. A. editor, *Fluid Interfacial Phenomena*, Wiley, New York, p. 45.

[12] Yatsyshin, P., Savva, N. and Kalliadasis, S. (2015), "Wetting of Prototypical One- and Two-Dimensional Systems: Thermodynamics and Density Functional Theory," *J. Chem. Phys.*, Vol. 142, p. 034708.

[13] Knepley, M. G., Karpeev, D. A., Davidovits, S., Eisenberg, R. S. and Gillespie, D. (2010), "An Efficient Algorithm for Classical Density Functional Theory in Three Dimensions: Ionic Solutions," *J. Chem. Phys.*, Vol. 132, p. 124101.

[14] Roth, R. (2010), "Fundamental Measure Theory for Hard-Sphere Mixtures: a Review," *J. Phys.: Condens. Matter*, Vol. 22, p. 063102.

[15] Frink, L. J. D., Salinger, A. G., Sears, M. P., Weinhold, J. D. and Frischknecht, A. L. (2002), "Numerical Challenges in the Application of Density Functional Theory to Biology and Nanotechnology," *J.Phys.: Condens. Matter*, Vol. 14, p. 12167.

[16] Frink, L. J. D. and Salinger, A. G. (2000), "Two- and Three-Dimensional Nonlocal Density Functional Theory for Inhomogeneous Fluids," *J. Comp. Phys.*, Vol. 159, p. 407.

[17] Reinhardt, J., Scacchi, A. and Brader, J. M. (2014), "Microrheology close to an equilibrium phase transition," *J. Chem. Phys.*, Vol. 140, p. 144901.

[18] Savva N. and Kalliadasis, S. (2009), "Two-Dimensional Droplet Spreading Over Topographical Substrates," *Phys. Fluids*, Vol. 21, p. 092102.

[19] Savva N. and Kalliadasis, S. (2011), "Dynamics of Moving Contact Lines: A Comparison Between Slip and Precursor Film Models," *Europhys. Lett.*, Vol. 94, p. 64004.

[20] Nold, A., Sibley, D. N., Goddard, B. and Kalliadasis, S. (2014), "Fluid Structure in the Immediate Vicinity of an Equilibrium Three-Phase Contact Line and Assessment of Disjoining Pressure Models Using Density Functional Theory," *Phys. Fluids*, Vol. 26, p. 072001.

[21] Boyd, J. P. (2001), *Chebyshev and Fourier Spectral Methods*, Dover Publications.

[22] Trefethen, L. N. (2000), *Spectral Methods in MATLAB*. SIAM.

[23] Hale, N. and Trefethen, L. N. (2008), "New Quadrature Formulas From Conformal Maps," *SIAM J. Numer. Anal.*, Vol. 46, p.930.

[24] Dhawan, S., Reimel, M. E., Scriven, L. E. and Davis, H. T. (1991), "Wetting Transitions at a Solid-Fluid Interface," *J. Chem. Phys.*, Vol. 94, p. 4479.

[25] Salinger, A. G. and Frink, L. J. D. (2003), "Rapid Analysis of Phase Behavior with Density Functional Theory. I. Novel Numerical Methods," *J. Chem. Phys.*, Vol. 118, p. 7457.

[26] Bonn, D. and Ross, D. (2001), "Wetting Transitions," *Rep. Prog. Phys.*, Vol. 64, p. 1085.

[27] Evans, R. and Marconi, U. M. B. (1987), "Phase Equilibria and Solvation Forces for Fluids Confined Between Parallel Walls," *J. Chem. Phys.*, Vol. 86, p. 7138.

[28] Rejmer, K., Dietrich, S. and Napiorkowski, M. (1999), "Filling Transition for a Wedge," *Phys. Rev. E*, Vol. 60, p. 4027.

[29] Parry, A. O., Rascon, C. and Wood, A. J. (1999), "Universality for 2D Wedge Wetting," *Phys. Rev. Lett.*, Vol. 83, p. 5535.

[30] Goddard, B., Nold, A., Savva, N., Pavliotis, G. A. and Kalliadasis, S. (2012), "General Dynamical Density Functional Theory for Classical Fluids," *Phys. Rev. Lett.*, Vol. 109, p. 120603.

[31] Goddard, B., Nold, A., Savva, N., Yatsyshin, P. and Kalliadasis, S. (2013), "Unification of Dynamic Density Functional Theory for Colloidal Fluids to Include Inertia and Hydrodynamic Interactions: Derivation and Numerical Experiments," *J. Phys.: Condens. Matter*, Vol. 25, p. 035101.